A novel calibration procedure of Johnson-Cook damage model parameters for simulation of scratch abrasion

Dhanraj Rajaraman[1*], Stijn Hertelé[1], Dieter Fauconnier[1]

[1] Soete Laboratory, Dept. EMSME, Ghent University, Belgium

*Corresponding author - Soete Laboratory, Department of ElectroMechanical, Systems and Metal Engineering (EMSME), Ghent University, Technologiepark-Zwijnaarde 46, 9052 Gent, Belgium

Dhanraj Rajaraman[1*] - Dhanraj.Rajaraman@UGent.be

Stijn Hertelé[1] - Stijn.Hertele@UGent.be

Dieter Fauconnier[1] - Dieter.Fauconnier@UGent.be

A novel calibration procedure of Johnson-Cook damage model parameters for simulation of scratch abrasion

Dhanraj Rajaraman[1*], Stijn Hertelé[1], Dieter Fauconnier[1]

[1] Soete Laboratory, Dept. EMSME, Ghent University, Belgium

Numerical simulation of scratch abrasion requires the use of a material damage model to simulate material degradation and removal. From our previous research, the stress state during scratch was found to show negative values of stress triaxiality and Lode angle parameter. However, models are "classically" calibrated using experiments with positive triaxiality and Lode angle parameter. In this work, a novel "scratch-based" calibration procedure is developed to acquire Johnson-Cook (JC) damage model parameters, using experimental scratch tests showing negative stress triaxiality and Lode angle parameter. An optimization procedure is used to obtain the parameters by minimizing the error between the experimental and numerical wear rates. Fracture loci obtained from both calibration procedures vary significantly, thus estimating different material losses. This highlights the importance of the calibration process of the damage model. The validity of the exponential Johnson-Cook fracture locus is questioned since it cannot account for accurate predictions under the entire range of stress triaxiality values covered in the paper. Hence, it may not be feasible for any calibration approach to obtain a single set of JC model parameters to accurately estimate the material loss for different cases of abrasion.

Keywords: Johnson-Cook damage model, Calibration, Finite element analysis, Scratch abrasion, Stress triaxiality, Lode angle parameter

*Corresponding author: Dhanraj.Rajaraman@UGent.be

1. Introduction

Scratch abrasion is an abrasive wear mechanism wherein a sharp and hard indenting body penetrates and slides through a typically softer material [1]. Focusing on ductile metallic materials, three major damage mechanisms govern scratch abrasion: ploughing, wedging and cutting [2,3]. Predicting the fundamental mechanism(s) and the severity of abrasion, either by experiments or simulations, is an ongoing challenge [1,3–8] due of the high sensitivity to specific operating conditions, material properties and microstructure.

Several experimental studies have investigated scratch abrasion [2,3,9,10]. Screening, analysing and ranking new materials solely on an experimental basis is practically infeasible due to the large number of influencing factors, the high number of experiments to obtain statistically sound results, and the labour and time to prepare and analyse the samples. Numerical analysis aims to bypass these limitations as it allows for extensive parametric studies. This requires an accurate model which is properly validated by experimental data, in terms of scratch depth and material loss. Continuum damage mechanics is often adopted hereto.

The reliability of any continuum damage model depends on its model parameters [11,12] and its ability to account for damage initiation and evolution. The majority of continuum damage models rely on the stress triaxiality, based on the first and second stress tensor invariant (i.e., hydrostatic stress and von Mises stress). The Johnson-Cook (JC) damage model is one of the most popular models used for damage initiation [7,8,13–15] and has been commonly applied for modelling and simulation of scratch abrasion. However, more recent damage models [16–19] have shown significant influences of the third deviatoric stress tensor invariant (the so-called Lode angle parameter) on material failure.

Numerous efforts towards numerical analysis of scratch abrasion have been undertaken using either mesh-based finite element modelling (FEM) [6–8,10,13–15,20,21], or meshless methods such as smooth particle hydrodynamics (SPH) [22], or the material point method (MPM) [23]. However, several limitations and shortcomings are identified in literature. A majority of studies [8,24–29] exclude damage and only include plasticity during scratch abrasion. Only few scratch-abrasion studies involve damage modelling, but typically they account only for the influence of stress triaxiality on the fracture strain, while ignoring the potential Lode angle dependence [7,13]. Furthermore, many authors rely on damage model parameters that are obtained from other sources in literature [7,13,15], or by using calibration experiments [7,13,15,22,23] that are characterized by a completely different stress state (e.g. tensile tests) which is not representative for scratch abrasion. At times, model parameters are used which were calibrated for a different material with different hardness and microstructure, and using these is strongly debatable [16]. On top of that, the mesh dependence of the classic damage models is often ignored since the small required element size required for abrasion simulations does not correspond to the coarser element size typically used in the calibration process, triggering potentially different damage behaviour [20,30,31]. Finally, the material loss (requiring damage modelling) is almost never investigated quantitatively in typical simulation studies [7,13,15], despite the fact that such quantitative predictive capabilities are the main driver for computational research. Despite its limitations, it has been shown that the JC damage model may produce qualitative results to a reasonable extent [7,8,13,14]. Nevertheless, the need to simulate the correct scratch morphology [7], and to correctly represent the dependence of fracture strain to the stress state during scratch [15] has been recognized. Moreover, it is important to perform the scratch tests at the similar microstructure [16] as that of calibration experiments.

In a recent study [32], scratch tests were used to determine the Johnson-Cook (JC) plasticity model parameters. A range of model parameters were simulated extensively to generate parameter maps, which can be used for determining the yield stress or hardening modulus, as a function of geometric scratch characteristics. It was shown that, once the yield stress is known from indentation hardness, a good estimate of the hardening modulus can be obtained without the need for tensile tests. However, in the current work, the authors focus on obtaining JC damage model parameters, additional to JC plasticity model parameters.

In this paper, the authors perform calibrations to obtain the JC damage model parameters to investigate the governing mechanisms of scratch abrasion. Hereto, the authors implemented damage based on two (numerical) calibration procedures:

- The state-of-the-art "classic" calibration procedure [16–18], which calibrates the JC damage model parameters from various experimentally tested specimen configurations that are in the range of positive stress triaxiality and Lode angle parameter.
- A novel "scratch-based" calibration procedure, which calibrates the JC damage model parameters against the experimental scratch response (with a limited set of experimental results based on a single indenter configuration) that are in range of negative values of stress triaxiality and Lode angle parameter. To the authors best knowledge, such a calibration procedure for damage models applicable to scratch abrasion, has not been yet reported in literature.

Firstly, the evolution of the stress state parameters involving damage is compared against simulated results without damage formulation from an a-priori study [33]. Then, the abrasion results are compared using the obtained JC damage parameter from both the "classic" and the novel "scratch-based" calibration procedures. Finally, the damage model parameters are used to investigate other indenter configurations, and the observed responses are critically discussed to motivate the choice of suitable JC damage model parameters for different damage modes associated with scratch abrasion.

2. Materials and methods

2.1 A brief discussion on basic definitions

Typically ductile damage models [17–19,34] are developed based on first invariant of the Cauchy stress tensor $[\sigma]$, and the second and third invariants of the corresponding deviatoric stress tensor. Denoting $\sigma_1, \sigma_2, \sigma_3$ as the principal stresses, the hydrostatic stress σ_m, the von Mises equivalent stress $\bar{\sigma}$ and the third invariant of deviatoric stress tensor *r* are respectively written as

$$\sigma_m = \frac{1}{3}(\sigma_1 + \sigma_2 + \sigma_3), \tag{1}$$

$$\bar{\sigma} = \sqrt{\frac{1}{2}[(\sigma_1 - \sigma_2)^2 + (\sigma_2 - \sigma_3)^2 + (\sigma_3 - \sigma_1)^2]}, \tag{2}$$

$$r = \left[\frac{27}{2}(\sigma_1 - \sigma_m)(\sigma_2 - \sigma_m)(\sigma_3 - \sigma_m)\right]^{\frac{1}{3}} \tag{3}$$

The majority of ductile damage models [17,35–37] include effects of the hydrostatic stress and von Mises stress on failure strain, in terms of their ratio which is referred to as stress triaxiality η, given by

$$\eta = \frac{\sigma_m}{\bar{\sigma}}. \tag{4}$$

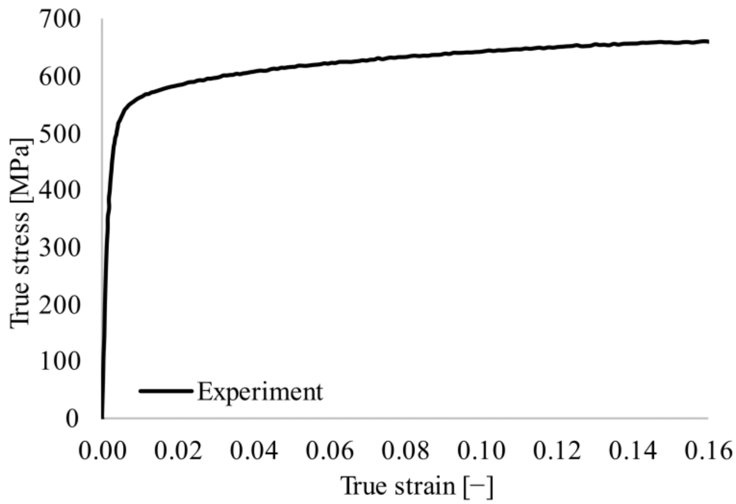

Fig. 1. Stress-strain curve of investigated material

The influence of the third stress tensor invariant on the failure strain $\bar{\varepsilon}_f$ has been included in ductile damage models in recent years with the definition of the Lode angle parameter $\bar{\theta}$ [17] as a function of the normalized third deviatoric stress invariant by Eq. (5),

$$\bar{\theta} = 1 - \frac{2}{\pi} \arccos \left(\frac{r}{\bar{\sigma}}\right)^3 \tag{5}$$

More information regarding the stress state parameters η and $\bar{\theta}$ can be found in [33].

2.2 Material model

2.2.1 Stress-strain behaviour

The availability of plasticity and fracture properties from the extensive experimental test program [16] led to the selection of X65 steel for the current study. A piece of the material tested in that paper was made available to the authors for scratch abrasion testing. The elastic properties of the material are listed in Table 1. The plastic part of the stress strain curve was extracted from uniaxial tensile tests performed on smooth round bar specimens in [16]. The resulting average true stress-true strain curve is shown in Fig. 1. For more information about the chemical composition, microstructure of the material, and the intensive experimental program, the authors refer to [16].

Table 1 Material properties of the X65 steel.

Elastic modulus	Poisson's ratio	Density	Hardness, Vickers HV30
GPa	-	kg/m^3	
210	0.3	7800	221

2.2.2 Damage initiation and evolution

To calculate the material loss during scratch abrasion, the numerical model should account for damage initiation and evolution. The phenomenological Johnson-Cook (JC) ductile damage model [36] is used as the damage initiation criterion. Further, for simplicity, thermal and strain rate effects have not been considered. Therefore, the JC model assumes the equivalent plastic strain at the onset of damage to be an exponential function of stress triaxiality with three model parameters $D_1 - D_3$:

$$\bar{\varepsilon}_D^{pl} = [D_1 + D_2 \exp{(D_3\,\eta)}] \tag{6}$$

When the damage initiation criterion is met, the damage evolution law (i.e., stiffness degradation up to complete failure) is based on the (effective) plastic displacement at failure $\bar{u}_f^{pl}$. This damage evolution law is defined as a linear function, wherein the damage variable $\dot{d}$ increases linearly with plastic displacement rate $\dot{u}^{pl}$, according to Eq. (7)

$$\dot{d} = \frac{L\dot{\varepsilon}^{pl}}{\bar{u}_f^{pl}} = \frac{\dot{u}^{pl}}{\bar{u}_f^{pl}} \tag{7}$$

where L is the characteristic element length (further referred to as element size). This definition ensures that when the effective plastic displacement $\bar{u}^{pl} = 0,$ the stiffness of the element is intact ($d = 0$), and when it reaches $\bar{u}_f^{pl}$, its stiffness will be completely degraded ($d = 1$).

2.3 Calibration methodology

Four model parameters need to be experimentally calibrated, the JC damage model parameters $D_1 - D_3$ (to model damage initiation) and $\bar{u}_f^{pl}$ (to model damage evolution). In the following, the "classic" calibration procedure for damage models – based on a number of calibration experiments characterized by a positive triaxiality and Lode angle – is described, followed by a newly proposed "scratch-based" calibration procedure – based on a set of scratch abrasion experiments. The stress state is shown in Fig. 2 for classic tests corresponding to fracture strain and for the scratch tests corresponding to the equivalent plastic strain value when the indenter is beneath the element. Both methods will be compared in the results section.

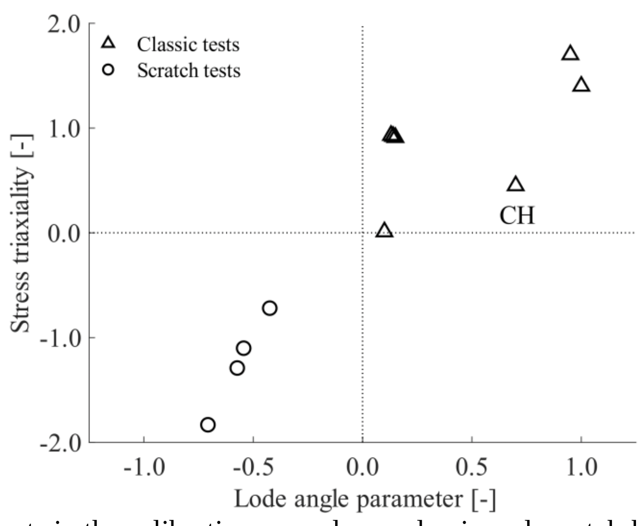

Fig. 2. Stress state of tests in the calibration procedures: classic and scratch-based. CH indicates central hole test.

2.3.2 The classic calibration procedure

The classic calibration procedure is explained in Fig. 4 (left). It utilizes a hybrid experimental-numerical approach [16–18] to obtain model parameters. The readily available results of X65 steel from the thorough experimental test program [16] were used to minimize the extensive calibration effort. The test program covers a range of stress states using a set of traditional tests such as notched tensile flat bars with different notch radii (NT20, NT10, NT6.67), central hole with 8 mm radius (CH), shear butterfly (BF-S) and notched tensile circular bars with different radii (NRB1, and NRB0.5).

A numerical model of every tested geometry was created, obeying an equally fine meshing strategy as the scratch abrasion simulation around the location of failure. Then, with the help of the stress-strain curve (shown in Fig. 1), the numerical load-displacement responses were evaluated against the experimental load-displacement responses. Furthermore, the evolution of stress triaxiality and the corresponding equivalent plastic strain at the failure locations were extracted for every specimen. Finally, the appropriate JC damage model parameters $D_1 - D_3$ (to model damage initiation) were evaluated by using a least square curve fitting method, by fitting the simulated stress triaxialities against the fracture strains from the experiment (Fig. 3).

The evolution of stress triaxiality and Lode angle parameter is negative during scratch abrasion [33]. Among the classic calibration tests indicated in Fig. 2, the stress state of the butterfly-shear test is relatively the closest to the stress state that occurs during scratch (shown in Fig. 2) (albeit still remote to the stress state during scratching). But, due to the unavailability of the damage evolution data of the butterfly-shear test, the centre-hole tension test (second closest to the stress state that occurs during scratch, indicated in Fig. 2) (given in [16]) is selected to determine the plastic displacement at failure $\bar{u}_f^{pl}$ (damage evolution) parameter. Then, a gradient free optimization procedure is used to obtain the appropriate plastic displacement at failure parameter by evaluating the minimum of an objective function given in Eq. (8), which evaluates the root mean square (RMS) difference between the experimental and numerical load-displacement responses.

$$Obj_F = \sqrt{\frac{1}{n}\sum_{i=1}^{n}\left(F_i^{exp} - F_i^{num}\right)^2} \tag{8}$$

where $F^{exp}$and F^{num} correspond to the experimental and numerical loads, and the objective function is evaluated at $n = 200$ equidistant data points i of displacement. It should be emphasized that the calibration is confined to the description of failure in the presence of a positive stress triaxiality.

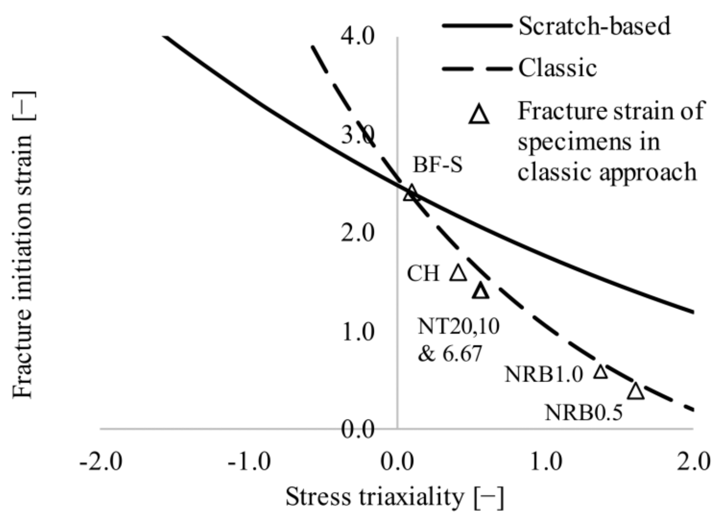

Fig. 3. Fracture locus from the calibration procedures: Classic and scratch-based. Triangle symbols represent the fracture strains of the tests used for the classic calibration [16].

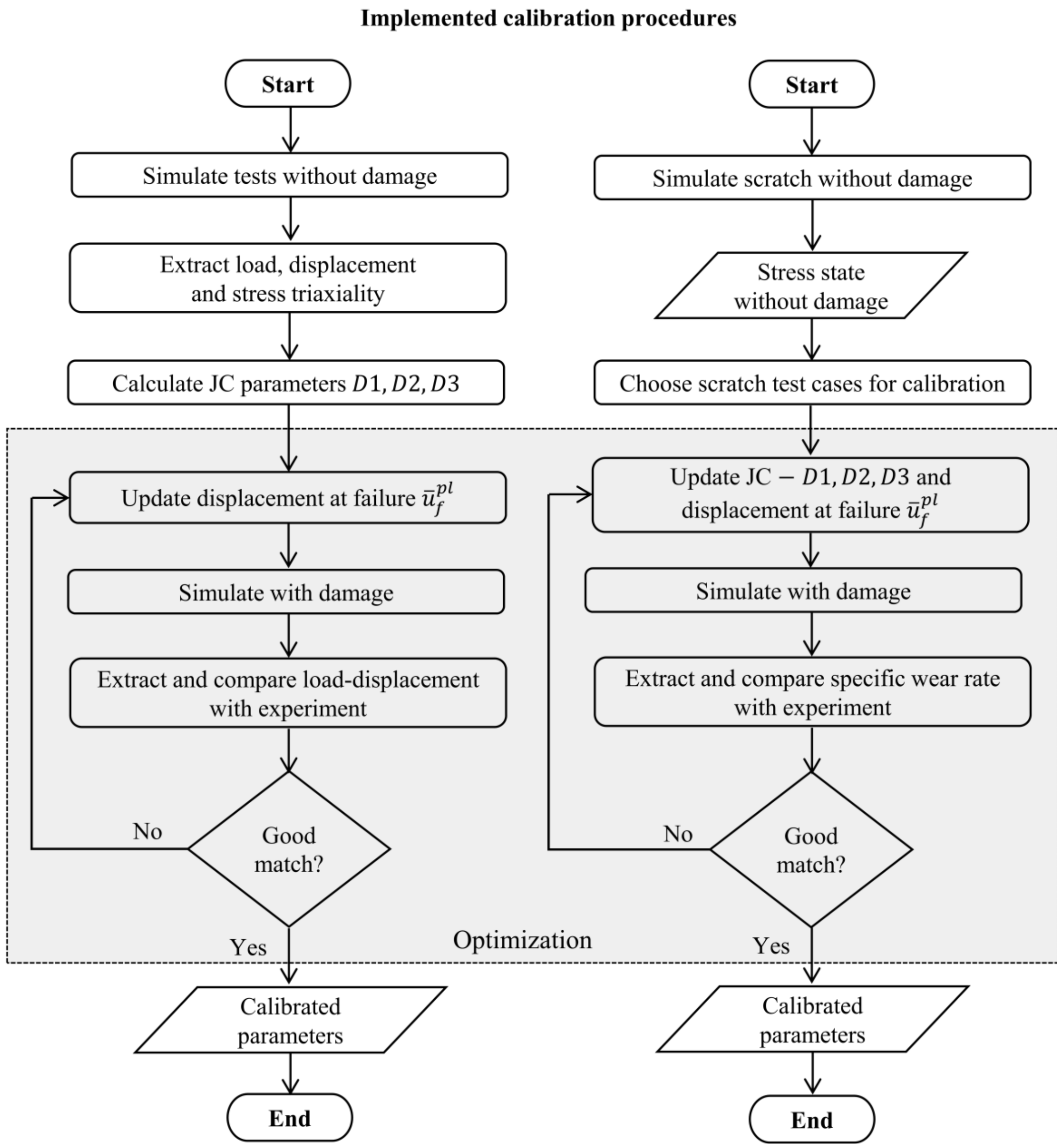

Fig. 4. Flowchart of calibration procedures for scratch abrasion: Classic (left) and scratch-based (right).

2.3.3 The scratch-based calibration procedure

The novel scratch-based calibration procedure is explained in Fig. 4 (right). It obtains model parameters such that scratch simulations optimally match with corresponding experiments. This method attempts to use a small set of scratch simulations for calibration that are well-chosen based on evolutions of stress triaxiality and Lode angle parameter obtained from plasticity simulations. Added to that, simulations spreading across different load levels were used to induce a wide range of stress trajectories. The agreement between experiments and simulations was compared on the basis of specific wear rate. As a result, contrary to the classically calibrated damage model, the calibration involves damage at stress states relevant to scratch abrasion, i.e., covering a range of negative stress triaxiality and Lode angle parameter values (Fig. 5).

The above-mentioned selection criteria are satisfied upon choosing scratch abrasion cases with a conical diamond indenter with a tip radius of $50\ \mu m$ and a cone angle of $120°$ and with loads between $1-12$ N. This range of conditions led to the observation of ploughing, wedging and cutting in subsets of the performed experiments. Selected cases within this load range were experimentally tested to obtain their respective material losses, which are used further in an objective function of the calibration. At the same time, numerical models of these selected cases were simulated.

A gradient free optimization procedure is used to obtain the four damage model parameters by minimizing an objective function that evaluates the root mean square relative error (RMSRE) between the experimental and numerical specific wear rates Eq. (9). By considering specific wear rate in the definition of the objective function, the simulation of quantitative material loss during scratch abrasion is optimized. Hereby, specific wear rate is calculated from simulations as defined in Eq (10). Notably, the experimental determination of specific wear rate (k^{exp}) is explained in the next section.

$$Obj_k = \frac{1}{N}\sqrt{\sum_{j=1}^{N}\left(\frac{k_j^{exp}-k_j^{num}}{k_j^{exp}}\right)^2} \tag{9}$$

where $k^{exp}$and k^{num} correspond to the experimental and numerical responses of specific wear rate and N refers to total number of load cases.

$$k^{num} = \frac{2\sum_{j=1}^{n} v.d_{ij}}{F.L} \quad \left[in\,\frac{\mu m^3}{N.\mu m}\right] \tag{10}$$

where v is the volume of an element j (which has a constant value in our model), d_{ij} is the normalized damage (between 0 and 1, the latter value representing element removal) at an element j, F corresponds to loads of tested cases, L corresponds to the scratch length, and a factor 2 accounts for the fact that only a half geometry was simulated due to symmetry.

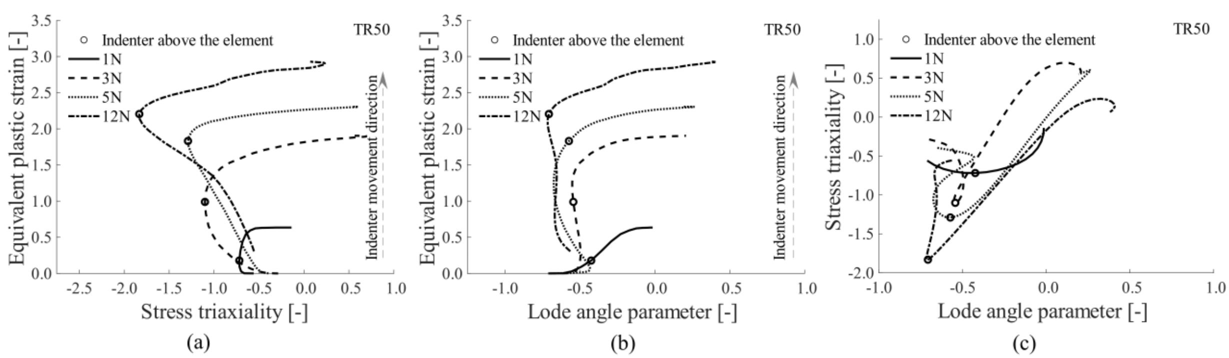

Fig. 5. Evolution of stress state parameters for simulations associated with different modes for the indenter tip radius of $50\ \mu m$

Key differences of the investigated calibration procedures are summarized in below Table 2. The scratch-based calibration procedure benefits from: (1.) utilizing the scratch tests themselves for calibration, therefore avoiding additional experiment types for validation and requiring a small volume of test material, (2.) as a result, the model parameters are calibrated in the more representative scratch abrasion stress state (which includes all three invariants), (3.) considering specific wear rate in the definition of the objective function, the model parameters can be calibrated based on material loss. Contrary to its advantages, the scratch-based procedure faces the challenge in terms of computationally expensive calibration simulations, which requires a lot of iterations to converge towards optimum model parameters.

Table 2 Key difference of both calibration procedures for scratch abrasion.

	Classic (in this study)	Scratch-based (in this study)
Stress state parameters		
Stress triaxiality	Yes	Yes
Lode angle parameter	−	Yes
Calibration	Yes	Yes
Stress state of the specimens are,	Positive	Negative
Experiments required	Various tests [16]	A limited set of scratch tests
Objective function	Min. (L − D)	Min. SWR
Damage		
Quantitative material loss	Yes	Yes

2.4 Experimental procedure: single pass scratch test

The surface of specimens for the single pass scratch tests was extracted at the same location as that of the calibration specimens from the classic calibration (see [16]) in order to reduce any impact of microstructural and hardness gradients within the steel on the result. Samples were mechanically polished to a mirror finish after which single pass scratch tests were performed by moving a vertically loaded indenter across the surface. The average initial surface roughness (S_a) of the test sample was $0.02 \pm 0.01\ \mu m$, as suggested by the ASTM G171 standard. Test parameters are listed in Table 3. The specific wear rate of scratch tests was calculated using white light interferometry, by dividing the wear volume by applied load and scratch length, according to Eqn. (11) [38]. The 3D surface profile (left) and 2D line profile (right) obtained from the white light interferometry is shown in Fig. 6. For a single scratch, a total of three 3D surface profile measurements were obtained and from a single measurement, a total of 2048 2D line profiles were extracted. The average line profile of the total extracted profiles (3 repeats, 9 times 2048 line profiles) were used to calculate the results. The position of the extracted 2D scratch profiles and the groove and ridge area is illustrated.

$$k = \frac{l(A_g - A_r)}{F.l} = \frac{A_g - A_r}{F} \quad \left[in \frac{\mu m^3}{N.\mu m}\right] \tag{11}$$

where A_g is the groove area, A_r is the ridge area, l is the scratch length and F is the applied load.

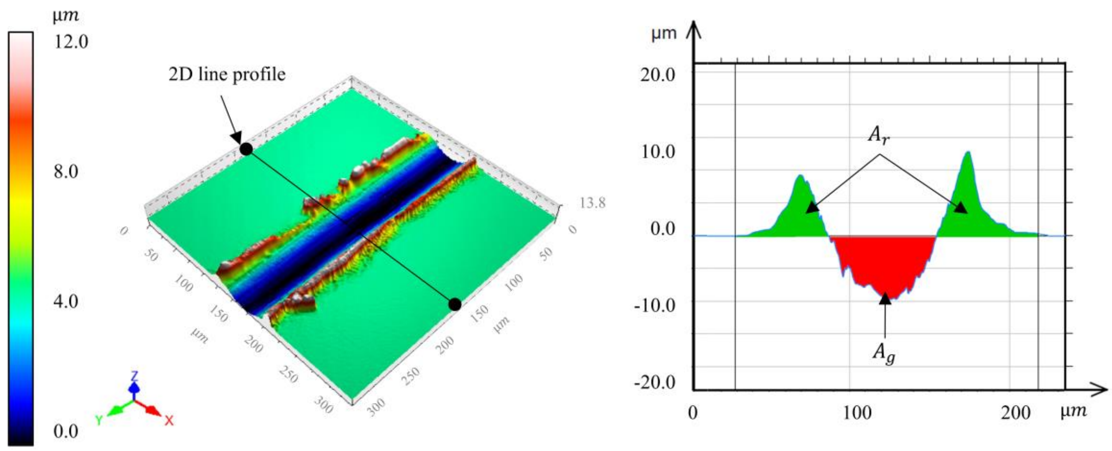

Fig. 6. Examples of 3D scratch surface (left) and 2D scratch profile (right) obtained using white light interferometry, illustrating ridge area (A_g, in green) and groove area (A_r, in red).

Table 3 Test conditions and indenter configurations of the scratch test.

		Units	Values
Indenters	Material		Diamond
	Cone angle	°	$60, 90, 120$
	Tip radius	μm	$50, 100, 200$
Test conditions	Load	N	$1 - 12$ (Step size of 1 N)
	Sliding velocity	mm/s	0.2
	Scratch length	mm	5
	Distance between scratches	mm	0.5
	Number of tests per condition		3

3. Numerical model

3.1 Description

An elastic-plastic scratch abrasion model was developed earlier [33,39] and was extended into a model that includes damage. The JC damage model was included to predict material loss during cutting and wedging. A linear damage evolution law (details in Sec. 2.2.2), readily available in ABAQUS/Explicit (2019), was adopted. The abraded region of interest has a structured mesh containing cubical elements with a fixed element size of 2 μm, leading to a volume v in Eq. (10) of 8 μm³. This value was chosen according to the minimum scratch depth obtained from the experiments (namely 1.617 μm) corresponding to the load level where damage is observed obtained for smoothest indenter with a tip radius of 200 μm. Away from the contact, a smaller mesh density was taken for computational efficiency. By using a fixed element size of 2 μm for all simulations, u_f as a material parameter and keeping the element aspect ratio to 1, the effect of mesh size on damage prediction is counteracted.

Rigid indenters with tip radii of $50, 100, 200$ μm were created. An element-based surface-to-surface contact interaction was defined between the indenter and the specimen with a friction coefficient of 0.1. When an element is completely damaged and removed (for example, in case of cutting), the indenter comes in contact with elements beneath the surface. As a result, the contact definition was extended to elements beneath the initial specimen surface. A scratch length of 1 mm was simulated for all simulations. This length provided a satisfactory balance between simulation time and the ability to overcome the transient behaviour at the

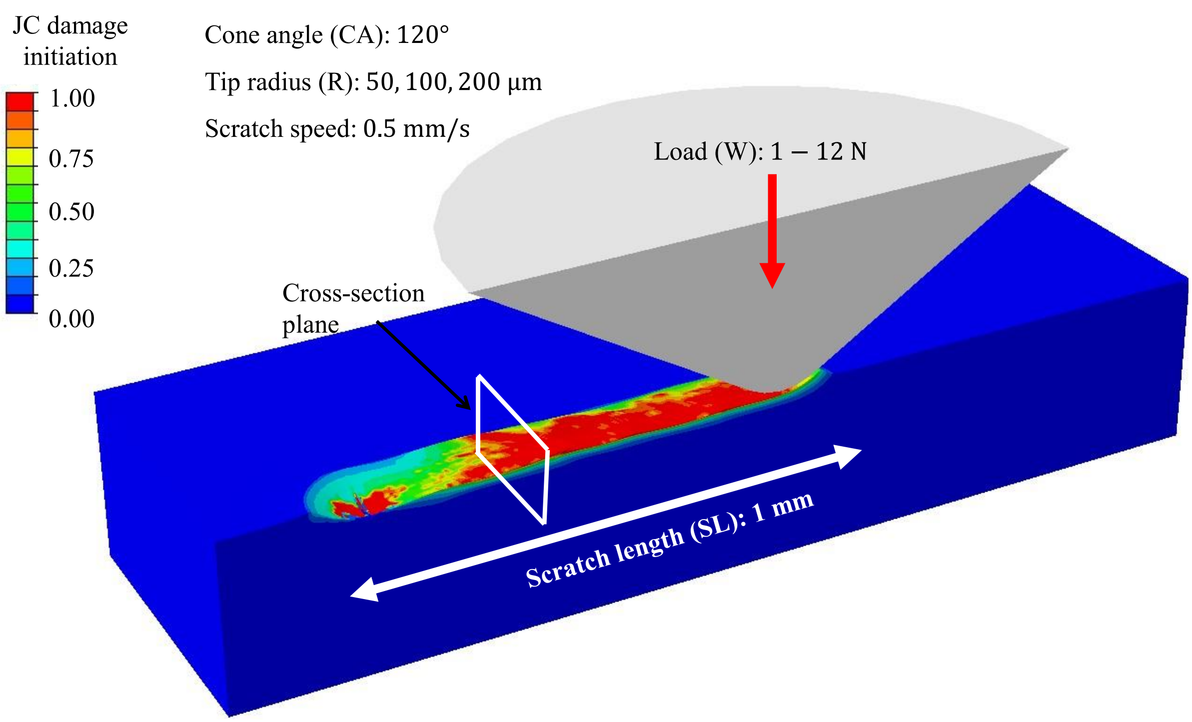

Fig. 7. Contour plot of von Mises stress from an example numerical simulation.

start of the indentation. The numerical model is shown in Fig. 7, and additional model details can be found in references [33,39].

4. Results

4.1 Experimental results: single pass scratch test

The objective function (Eq. (9)) requires the material loss from experimental scratch tests. To this end, the specific wear rate was obtained from the experimental results of all indenter geometries (shown in Fig. 8b) for different load levels. Error bars indicate one standard deviation on both sides of the mean from three tests.

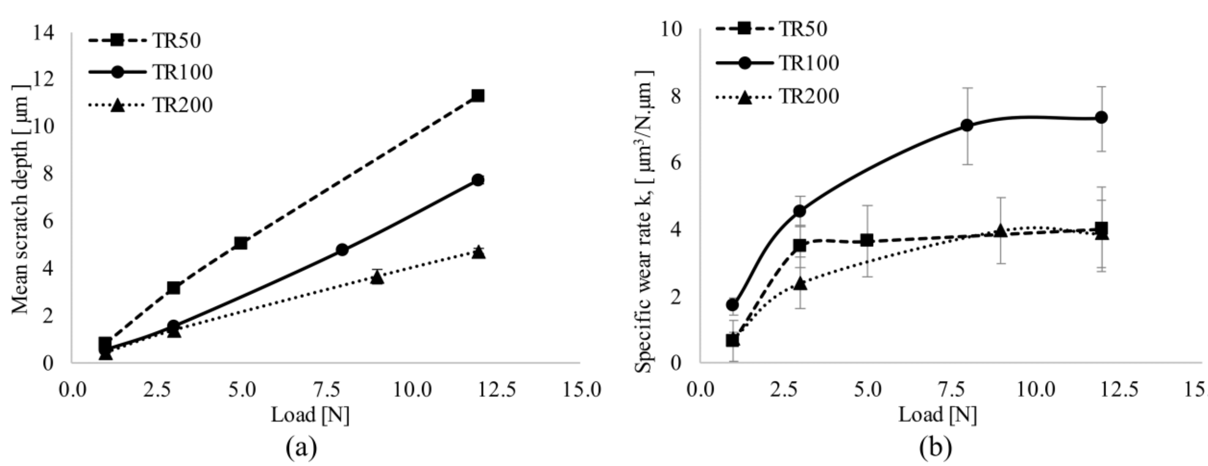

Fig. 8. Experimental results of single pass scratch tests. Mean scratch depth (a), specific wear rate (b), average ridge and groove area (c) of all indenter geometries

Mean scratch depth increases with an increase in load and a decrease in tip radius (Fig. 8a). For example, the mean scratch depth increased from 0.86 µm to 11.31 µm for the sharpest indenter (tip radius of 50 µm) when the load is increased from 1 to 12 N, and this sharpest indenter has a higher mean scratch depth in comparison to relatively blunt indenters. Meanwhile, specific wear rate (Fig. 8b) increases with increase in load and tends to stabilise at higher loads for all indenter geometries. The specific wear rate is observed to be highest for the indenter tip radius of 100 µm. This may be due to a critical tip size effect wherein the wear rate increases with asperity size until a critical size, beyond which the wear rate may manifest in different trend [40]. In literature [41,42], this critical tip size effect has been observed for steels. In addition, the geometric transition depth was measured from SEM micrographs of the indenter, which indicated that the geometric transition depth is relatively higher than the scratch depth (except for the load of 12 N, tip radius of 50 µm and 100 µm). Thus, the attack angle is not affected by the cone angle.

4.2 Calibration results

4.2.1 Fracture loci from the calibration procedures

The results for both calibration procedures are presented in Fig. 3 and Table 4. The fracture initiation strain locus calibrated to the classic experimental dataset is marked by triangle symbols. The associated plastic displacement at failure was acquired from an optimization procedure using the centre-hole specimen, based on the experimental and numerical load-displacement responses. As the damage evolution parameter is mesh dependent (as shown in Eqn. (7)), the plastic displacement at failure was acquired for an element size of 2 µm and has been held same for scratch abrasion simulations.

As regards the scratch-based model parameter calibration, convergence is reached for which the root mean square relative error was reduced by 4 times from the initial value to a best estimate of 0.1. However, the residual stagnated at 0.1. We conclude that the lack of convergence is because no unique set of parameters ($D_1 - D_3$ and $\bar{u}_f^{pl}$) can be found for which the JC damage model is capable of fitting all four scratch abrasion simulations properly during the calibration. This implies that the JC damage model does not properly describe the fracture locus for stress states relevant in scratch abrasion. The model parameters corresponding to the best estimate of 0.1 is henceforth considered as the best possible value of the scratch-based calibration using the JC model.

Table 4 Calibrated Johnson-Cook (JC) damage model parameters of the tested X65 steel.

	Damage initiation Parameters			Damage evolution Parameter
	D_1	D_2	D_3	Plastic displacement at failure, $\bar{u}_f^{pl}$
Classic approach	-0.9252	3.4998	-0.5646	0.0180
Scratch-based approach	-1.0452	3.5398	-0.2280	0.0192
Difference in %	12.180	1.1300	84.920	6.4500

For the cases simulated in this paper, the fracture locus obtained using the scratch-based calibration is significantly flatter in comparison with that obtained from the classic calibration method. Both appear to have a similar fracture strain for zero stress triaxiality. As a consequence, the scratch-based calibration procedure indicates lower fracture initiation strains for negative stress triaxiality values, in comparison to the classic calibration. This implies that a classically calibrated JC model would underpredict the specific wear rate, compared to the model calibrated on the basis of scratch simulations. Likewise, the scratch-based calibration procedure – containing exclusively scratch tests with negative triaxiality and Lode angle – would not provide reliable damage model parameters for cases with positive triaxiality. This indicates that the exponential form of the Johnson-Cook failure locus is not suitable when considering the entire triaxiality range from negative to positive values. Additionally, it can be argued that the disagreement between fracture loci could also be because of differences in Lode angle parameter between the calibration tests with positive triaxiality and the scratch abrasion tests. Since the JC model does not account for the influence of Lode angle parameter on fracture strain, the potential effect of such differences cannot be accounted for. We do note that, from the reported tests that led to the “classic” calibration, no markable effect of Lode angle parameter on the exponential shape of the fracture locus was observed for positive triaxialities, for the material investigated in this paper.

4.2.2 Specific wear rate and mean scratch depth

In order to evaluate the differences in scratch abrasion wear predicted after executing both calibration procedures, the simulations used for the scratch based calibration (adopting an indenter tip radius of 50 μm) were repeated, using both sets of model parameters listed in Table 4. Resulting specific wear rates were compared against the corresponding experimental results (Fig. 9a). Despite the good agreement of the specific wear rate at low loads, the values are slightly overestimated for higher loads and in particular at 12 N, which is a case where material loss is due to cutting. Nonetheless, the simulated wear rate after scratch-based calibration falls within the scatter band of experimental results for all simulated values.

However, when performing scratch simulations with both model parameter sets for indenter tip radii of respectively 100 μm and 200 μm, the scratch-based parameter set leads to significantly higher material losses than the classic parameter set, but (strongly) underestimates the experimental data. This shows that a single parameter set calibrated using a single indenter geometry may not be able to accurately describe damage for other indenter geometries.

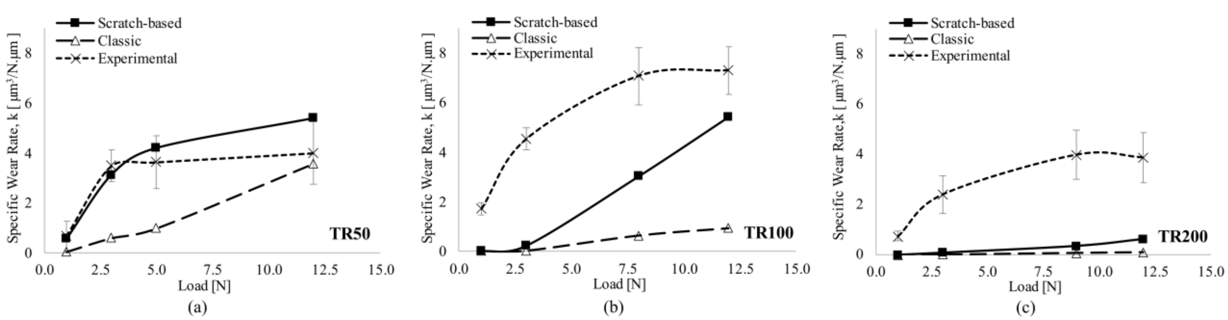

Fig. 9. Specific wear rate (material loss) from both calibration procedures for a tip radius of 50 μm (a), 100 μm (b), 200 μm (c).

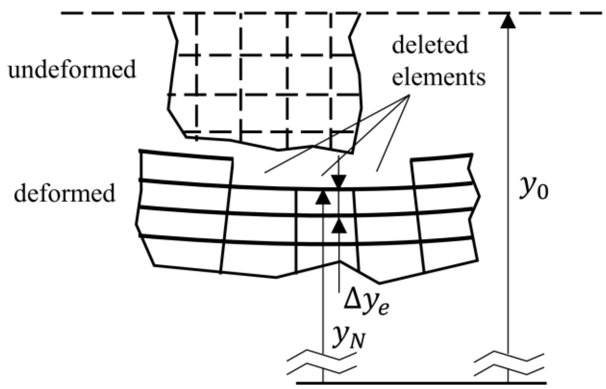

Fig. 10. Representative figure for the calculation of scratch depth from simulations with damage.

In addition to specific wear rates, mean scratch depths were obtained from simulations as the average post-mortem indentation depth along the scratch path. For any given position along this scratch path, this depth was calculated using Eq. (12),

$$\delta = y_0 - y_N - d \,.\, \Delta y_e \tag{12}$$

Fig. 10 shows the terms used in the calculation of scratch depth δ from the simulations with damage. y_0 is the position of the undamaged surface, and y_N is the position of the first element touching the surface (after potential deletion of elements due to damage). Considering that this element may be partially damaged with a value d (between 0 and 1), a corresponding portion of the height of that element Δy_e is also included in the calculation of scratch depth to compensate for partial removal. We emphasize that this calculation is consistent with the definition of the specific wear rate, used for calibration. The mean scratch depth and its standard deviation were obtained over the middle part of the scratch length, which is considered not to be influenced by the run-in and run-out.

Results for simulations using both damage model calibration procedures are shown in Fig. 11 in comparison to the experimental and model predictions in absence of a damage formulation (denoted as "plasticity"). There is a good agreement between the experimental and simulated scratch depths. Remarkably, the mean scratch depths obtained using the JC damage model with both calibration procedures are comparable to the mean scratch depths from elastic-plastic simulations. The relative insensitivity of scratch depth to damage development, and the potential unevenness of simulated scratch profiles indicate that scratch depth is a poor metric for the purpose of the scratch-based damage model calibration, in contrast to material loss.

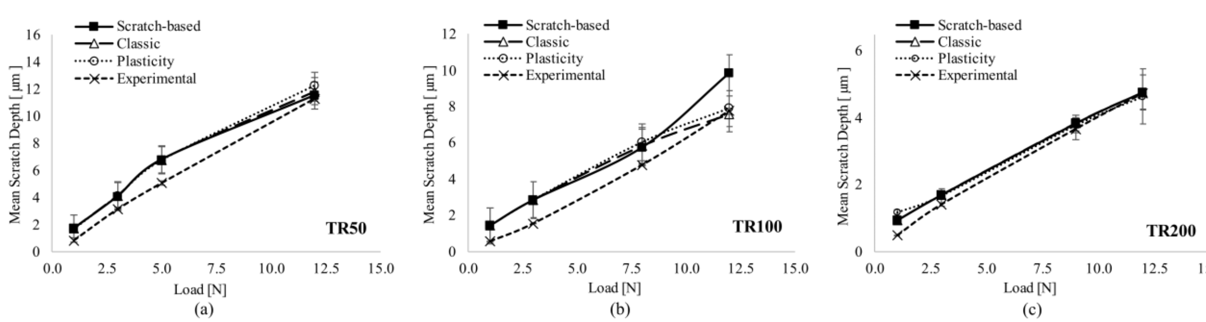

Fig. 11. Mean scratch depth from both calibration procedures for a tip radius of 50 μm (a), 100 μm (b), 200 μm (c).

4.2.3 Evolutions of stress state

Stress state trajectories for three different simulations are shown in Fig. 12. According to the corresponding experimental results, each simulation is associated with a different predominant mode of abrasion (ploughing, wedging, and cutting). The figure compares the stress state trajectories obtained using the JC damage method with those from an elastic-plastic simulation without damage, as performed in previous work [33].

For all three cases, simulated stress state trajectories are similar with and without damage modelling. In front of the indenter, at the onset of plasticity, the levels of stress triaxiality and Lode angle are negative. As the indenter approaches, the equivalent plastic strain increases steeply with decreasing stress triaxiality and reaches a minimum value of triaxiality when the indenter is just on top of the monitored element. For the majority of the plastic strain development, the Lode angle parameter varies between -0.6 to -0.5. Behind the indenter, equivalent plastic strain increases slightly and eventually reaches a constant value, while the stress triaxiality and the Lode angle parameter increase drastically. We refer to our prior study [33] for a more in-depth analysis of these stress state trajectories. Closer inspections of the simulations using damage modelling indicated that the majority of damage development has occurred in front of and beneath the indenter, and only a minimal amount of damage development has occurred behind the indenter.

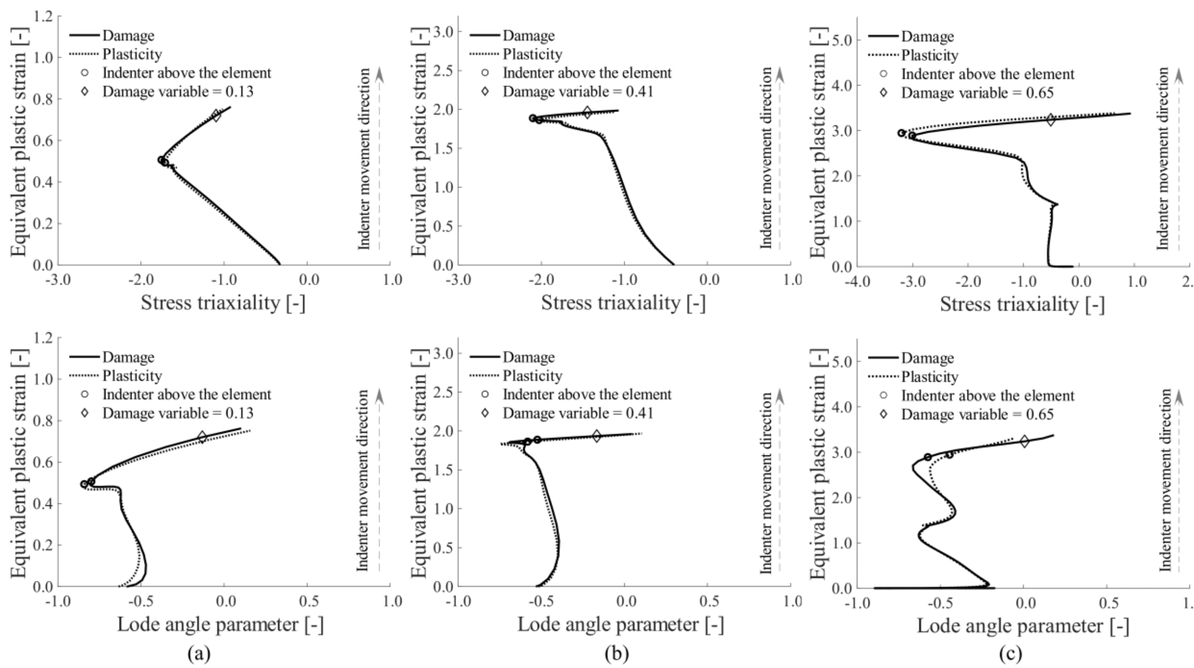

Fig. 12. Evolution of stress state parameters with and without damage model for a tip radius of 100 μ*m*, for ploughing – 1 N (a), wedging – 3 N (b), and cutting – 12 N (c).

4.3 Sensitivity of model parameters for scratch abrasion

A (parametric) sensitivity study of scratch abrasion behavior with respect to the damage model parameters has been performed based, using the parameters from the scratch-based calibration as a reference. By doing so, effects of the position and the average slope of the JC fracture locus were investigated, and these are discussed below. From this point forward, the reference fracture locus is referred to as the scratch-based locus (SBL).

4.3.1 Effect of individual damage model parameters for an indenter with tip radius of 50 μm

In a first set of simulations, one distinct parameter was changed with respect to the SBL. The obtained fracture loci and the percentage difference with respect to the reference fracture locus are indicated in Fig. 13. While the JC-parameter D_1 controls the offset of the fracture locus and the parameter D_3 controls the average slope of the fracture locus, the parameter D_2 controls both the offset and the average slope of the fracture locus. Hereby, the influence of the model parameter D_2 on the fracture initiation strain appears to be significantly greater than that of model parameters D_1 and D_3.

For the tip radius of 50 μm, associated specific wear rates were estimated (Fig. 14). The fracture locus with increased D_1 and D_2 (SBL+20% and SBL+10% respectively) estimated lower material loss for all load levels in comparison to the scratch-based locus. This is consistent with the expectations as the fracture locus (Fig. 14a and Fig. 14b) shifted vertically upward has a higher fracture initiation strain, and therefore, decreased damage development (and material loss). Meanwhile, with decreased D_1 and D_2 (SBL-20% and SBL-10% respectively), the opposite can be observed. Similar behaviour can be observed with reduced D_3 (SBL-20%) wherein a lower material loss is estimated for all load levels. This is because the average slope of fracture locus (Fig. 13c) has increased, causing a higher fracture initiation strain, and therefore, decreased damage development (and thus material loss). This is further scrutinized for three abrasion modes in other indenter geometries with a tip radius of 100 and 200 μm.

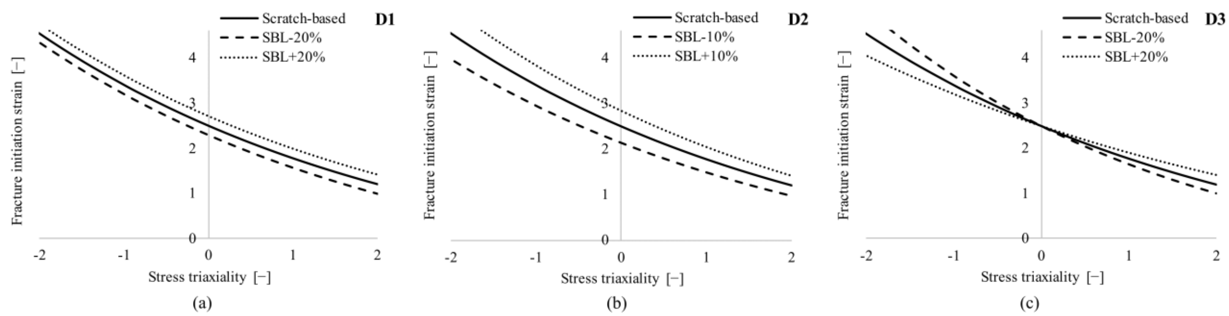

Fig. 13. Fracture loci from the sensitivity study, varying model parameters D_1 (a), D_2 (b), D_3 (c). SBL represents the scratch-based locus.

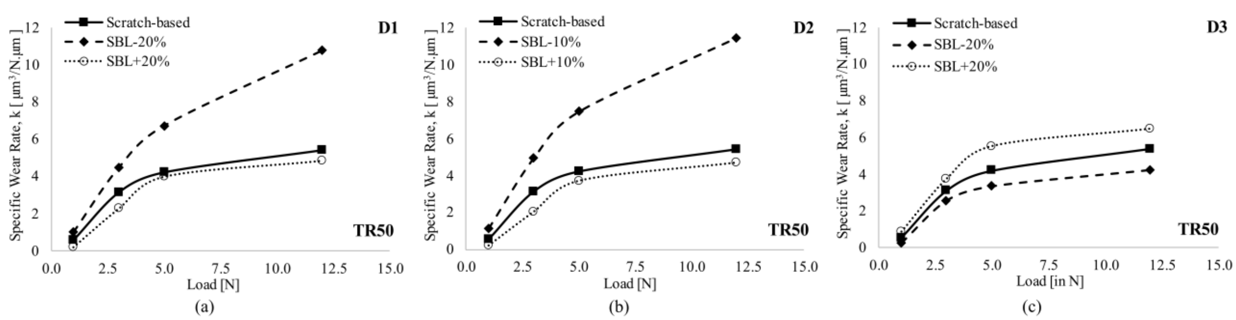

Fig. 14. Estimated specific wear rates from the sensitivity study for an indenter with tip radius of 50 μm, varying model parameters D_1 (a), D_2 (b), D_3 (c).

4.3.2 Effect of model parameter D_2 for indenters with different tip radii

In the previous section, the relative influence of model parameter D_2 on the fracture initiation strain was shown to be greater than that of model parameters D_1 and D_3. Moreover, as discussed in Sec 4.2.2, scratch-based fracture locus underpredicted the material loss for scratch abrasion with tip radii of 100 and 200 μm. Therefore, the material losses of both tip radii were investigated for different (decreased) D_2 values (Fig. 15a). Obtained specific wear rates are shown (Fig. 15b, c).

For both tip radii of 100 and 200 μm, the fracture locus with decreased D_2 (SBL-20% and SBL-10%) triggered higher material loss for all load levels in comparison to the scratch-based locus. This is because the fracture locus (Fig. 15a) has been shifted vertically downward, triggering a lower fracture initiation strain, and therefore, increased damage development (and material loss).

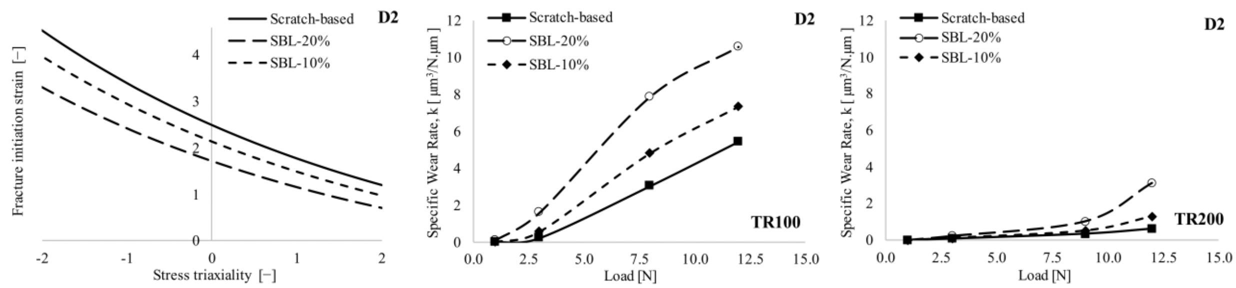

Fig. 15. Fracture loci based on variations of model parameter D_2 (a), associated specific wear rates for a tip radius of 100 μm (b), and 200 μm (c).

5. Conclusion

In this paper, scratch abrasion simulations were performed using a Johnson-Cook damage model, calibrated according to two procedures: one based on common testing to calibrate such model ("classic"), and the other based on scratch abrasion tests. The obtained simulation results were compared to purely elastic-plastic simulations (without damage), and to experimental scratch abrasion test results (covering more cases than covered in the scratch-based calibration). The following can be concluded.

Taking material damage into account using the JC model, did not alter the stress state trajectories at the surface of scratch abrasion simulations. Hence, conclusions drawn from an a-priori investigation of stress state evolution [33] remain valid.

For the cases studied in this work, the fracture loci obtained from the classic and scratch-based calibration procedures vary significantly from one another. The fracture locus obtained using scratch-based calibration has a smaller average inclination in comparison with that obtained from the classic calibration method, resulting in earlier damage initiation and subsequently an increased specific wear rate, i.e., higher material loss. The mean scratch depth in the cases studied was observed to be dominated by plastic deformation and is hence a poor metric for the purpose of the scratch-based damage model calibration.

In this work, several difficulties were encountered in finding a unique set of converged model parameters that could effectively fit the Johnson-Cook model calibration cases, under the entire range of negative stress triaxiality values that occur during various cases of scratch abrasion. Hence, we suggest further investigation into the suitability of damage models for simulation scratch abrasion.

Acknowledgement

The authors acknowledge Prof. Junhe Lian from Aalto University for providing test data from the calibration experiments, and ir. Naveenkumar Rajendhran for support in the experimental scratch tests. Also, the authors thank Ghent University for the financial support to perform this research.

Bibliography

[1] M.A. Moore, A Review of Two-Body Abrasive Wear, Wear. 27 (1974) 1–17. https://doi.org/10.1016/0043-1648(74)90080-5.

[2] K. Hokkirigawa, K. Kato, An experimental and theoretical investigation of ploughing, cutting and wedge formation during abrasive wear, Tribology International. 21 (1988) 51–57. https://doi.org/10.1016/0301-679X(88)90128-4.

[3] K. Hokkirigawa, K. Kato, Z.Z. Li, The effect of hardness on the transition of the abrasive wear mechanism of steels, Wear. 123 (1988) 241–251. https://doi.org/10.1016/0043-1648(88)90102-0.

[4] J. Hardell, A. Yousfi, M. Lund, L. Pelcastre, B. Prakash, Abrasive wear behaviour of hardened high strength boron steel, Tribology - Materials, Surfaces & Interfaces. 8 (2014) 90–97. https://doi.org/10.1179/1751584X14Y.0000000068.

[5] J.D. Gates, Two-body and three-body abrasion: A critical discussion, Wear. 214 (1998). https://doi.org/10.1016/S0043-1648(97)00188-9.

[6] M. Barge, G. Kermouche, P. Gilles, J.M. Bergheau, Experimental and numerical study of the ploughing part of abrasive wear, Wear. 255 (2003) 30–37. https://doi.org/10.1016/S0043-1648(03)00159-5.

[7] M. Woldman, E.V.D. Heide, T. Tinga, M.A. Masen, A Finite Element Approach to Modeling Abrasive Wear Modes, Tribology Transactions. 60 (2017) 711–718. https://doi.org/10.1080/10402004.2016.1206647.

[8] P. Wechsuwanmanee, J. Lian, J. Sukumaran, Á. Kalácska, H.B. Hamouda, P. De Baets, S. Münstermann, Finite Element Model in Abrasion Analysis for Single-Asperity Scratch Test, in: Proceedings of the 7th International Conference on Fracture Fatigue and Wear, 2019: pp. 768–779. https://doi.org/10.1007/978-981-13-0411-8_68.

[9] K.-H.Z. Gahr, Wear by hard particles, Tribology International. 31 (1998) 587–596. https://doi.org/10.1016/S0301-679X(98)00079-6.

[10] A. D'Acunto, G. Le Coz, A. Moufki, D. Dudzinski, Effect of Cutting Edge Geometry on Chip Flow Direction – Analytical Modelling and Experimental Validation, Procedia CIRP. 58 (2017) 353–357. https://doi.org/10.1016/j.procir.2017.03.327.

[11] J. Wang, W. Guo, J. Guo, Z. Wang, S. Lu, The Effects of Stress Triaxiality, Temperature and Strain Rate on the Fracture Characteristics of a Nickel-Base Superalloy, Journal of Materials Engineering and Performance. 25 (2016) 2043–2052. https://doi.org/10.1007/s11665-016-2049-9.

[12] T. Wierzbicki, Y. Bao, Y.-W. Lee, Y. Bai, Calibration and evaluation of seven fracture models, International Journal of Mechanical Sciences. 47 (2005) 719–743. https://doi.org/10.1016/j.ijmecsci.2005.03.003.

[13] F. Elwasli, F. Zemzemi, A. Mkaddem, S. Mzali, S. Mezlini, A 3D multi-scratch test model for characterizing material removal regimes in 5083-Al alloy, Materials & Design. 87 (2015) 352–362. https://doi.org/10.1016/j.matdes.2015.07.121.

[14] M. Ben Tkaya, H. Zahouani, S. Mezlini, Ph. Kapsa, M. Zidi, A. Dogui, The effect of damage in the numerical simulation of a scratch test, Wear. 263 (2007) 1533–1539. https://doi.org/10.1016/j.wear.2007.01.083.

[15] Akbar mostani, Comparison of Ductile Damage Models During Scratch Tests - A Numerical Study, in: The 8th International Conference BALTTRIB'2015, 2015. https://doi.org/10.15544/balttrib.2015.23.

[16] M. Paredes, J. Lian, T. Wierzbicki, M.E. Cristea, S. Münstermann, P. Darcis, Modeling of plasticity and fracture behavior of X65 steels: seam weld and seamless pipes, International Journal of Fracture. 213 (2018) 17–36. https://doi.org/10.1007/s10704-018-0303-x.

[17] Y. Bai, T. Wierzbicki, A new model of metal plasticity and fracture with pressure and Lode dependence, International Journal of Plasticity. 24 (2008) 1071–1096. https://doi.org/10.1016/j.ijplas.2007.09.004.

[18] Y. Bai, T. Wierzbicki, Application of extended Mohr–Coulomb criterion to ductile fracture, International Journal of Fracture. 161 (2010) 1–20. https://doi.org/10.1007/s10704-009-9422-8.
[19] J. Lian, A generalised hybrid damage mechanics model for steel sheets and heavy plates, Doctoral dissertation, RWTH Aachen university, 2015.
[20] M. Barge, H. Hamdi, J. Rech, J.-M. Bergheau, Numerical modelling of orthogonal cutting: influence of numerical parameters, Journal of Materials Processing Technology. 164–165 (2005) 1148–1153. https://doi.org/10.1016/j.jmatprotec.2005.02.118.
[21] M. Lindroos, Experimental and Numerical Studies on the Abrasive and Impact Behavior of Wear Resistant Steels, Doctoral dissertation, Tampere University of Technology, 2016.
[22] M. Varga, S. Leroch, S.J. Eder, M.R. Ripoll, Meshless microscale simulation of wear mechanisms in scratch testing, Wear. 376–377 (2017) 1122–1129. https://doi.org/10.1016/j.wear.2016.11.023.
[23] M. Varga, S. Leroch, S.J. Eder, H. Rojacz, M.R. Ripoll, Influence of velocity on high-temperature fundamental abrasive contact: A numerical and experimental approach, Wear. 426–427 (2019) 370–377. https://doi.org/10.1016/j.wear.2018.12.013.
[24] J.L. Bucaille, E. Felder, G. Hochstetter, Mechanical analysis of the scratch test on elastic and perfectly plastic materials with the three-dimensional finite element modeling, Wear. 249 (2001) 422–432. https://doi.org/10.1016/S0043-1648(01)00538-5.
[25] F. Wredenberg, P. Larsson, Experimental and numerical analysis of the scratch test, in: WIT Transactions on Engineering Sciences, 2005: pp. 251–261.
[26] E. Felder, J.-L. Bucaille, Mechanical analysis of the scratching of metals and polymers with conical indenters at moderate and large strains, Tribology International. 39 (2006) 70–87. https://doi.org/10.1016/j.triboint.2005.04.005.
[27] Subhash, Investigation of the overall friction coefficient in single-pass scratch test, Wear. 252 (2002) 123–134. https://doi.org/10.1016/S0043-1648(01)00852-3.
[28] J. Li, W. Beres, Three-dimensional finite element modelling of the scratch test for a TiN coated titanium alloy substrate, Wear. 260 (2006) 1232–1242. https://doi.org/10.1016/j.wear.2005.08.008.
[29] Guillaume Kermouche, Jean-Luc Loubet, Jean-Michel Bergheau, A 3D finite element procedure for modeling scratch test, in: International Conference Metrology and Properties of Engineering Surfaces, 2005: pp. 311–319.
[30] R. Ambati, H. Yuan, FEM mesh-dependence in cutting process simulations, The International Journal of Advanced Manufacturing Technology. 53 (2011) 313–323. https://doi.org/10.1007/s00170-010-2818-9.
[31] B. Erice, F. Gálvez, A coupled elastoplastic-damage constitutive model with Lode angle dependent failure criterion, International Journal of Solids and Structures. 51 (2014) 93–110. https://doi.org/10.1016/j.ijsolstr.2013.09.015.
[32] S. Leroch, S.J. Eder, M. Varga, M. Rodríguez Ripoll, Material point simulations as a basis for determining Johnson–Cook hardening parameters via instrumented scratch tests, International Journal of Solids and Structures. 267 (2023) 112146. https://doi.org/10.1016/j.ijsolstr.2023.112146.
[33] D. Rajaraman, V. Keim, K. Pondicherry, A. Nonn, S. Hertelé, D. Fauconnier, Stress state characterization of ductile materials during scratch abrasion, Wear. (2021) 203712. https://doi.org/10.1016/j.wear.2021.203712.
[34] P. Kubík, F. Šebek, J. Hůlka, J. Petruška, Calibration of ductile fracture criteria at negative stress triaxiality, International Journal of Mechanical Sciences. 108 (2016) 90–103. https://doi.org/10.1016/j.ijmecsci.2016.02.001.
[35] Y. Bao, Prediction of ductile crack formation in uncracked bodies, Massachusetts Institute of Technology, 2003.
[36] G.R. Johnson, W.H. Cook, Fracture characteristics of three metals subjected to various strains, strain rates, temperatures and pressures, Engineering Fracture Mechanics. 21 (1985) 31–48. https://doi.org/10.1016/0013-7944(85)90052-9.

[37] J.R. Rice, D.M. Tracey, On the ductile enlargement of voids in triaxial stress fields∗, Journal of the Mechanics and Physics of Solids. 17 (1969) 201–217. https://doi.org/10.1016/0022-5096(69)90033-7.
[38] J.F. Archard, Contact and Rubbing of Flat Surfaces, Journal of Applied Physics. 24 (1953) 981–988. https://doi.org/10.1063/1.1721448.
[39] K.S. Pondicherry, D. Rajaraman, T. Galle, S. Hertelé, D. Fauconnier, P. De Baets, Optimization and validation of a load-controlled numerical model for single asperity scratch, Tribology Letters. 68 (2020). https://doi.org/10.1007/s11249-020-1283-3.
[40] J.J. Coronado, A. Sinatora, Effect of abrasive size on wear of metallic materials and its relationship with microchips morphology and wear micromechanisms: Part 1, Wear. 271 (2011) 1794–1803. https://doi.org/10.1016/j.wear.2011.01.078.
[41] M. Woldman, E. Van Der Heide, T. Tinga, M.A. Masen, The influence of abrasive body dimensions on single asperity wear, Wear. 301 (2013) 76–81. https://doi.org/10.1016/j.wear.2012.12.009.
[42] K.S. Pondicherry, Two-Body Abrasion and Synergy in Abrasion-Corrosion of Martensitic and Complex Phase Steel, Doctoral dissertation, Ghent University, 2020.